communications earth & environment

ARTICLE

https://doi.org/10.1038/s43247-023-00903-5 OPEN

Pressure-driven processes explain the decreasing magnetization of the subducting oceanic crust in the Japan Trench

Dongwoo Han [1], Yong-Hee Park [2] & Changyeol Lee [1✉]

Despite the decreases in temperature and permeability of oceanic plates with increasing age, hydrothermal circulation (HC) can be rejuvenated in the 130-Ma old Pacific plate in the vicinity of the Japan Trench, substantially affecting the thermal structure and remaining amount of magnetization (RAM). To decipher the roles of HC in the thermal structure and the RAM, the vigor and extent of HC in the vicinity of the Japan Trench should be quantitatively evaluated. Here we numerically show that HC is rejuvenated in the outer-rise zone but ceases after subduction owing to permeability evolution. The calculated thermal structure explains the measured heat flow evolution but negates the HC-driven thermal demagnetization, which was thought to decrease the RAM after subduction. Instead, we propose that the pressure-driven processes decrease the RAM after subduction through the demagnetizations of titanomaghemite and magnetite and the mineral phase transitions from maghemite to hematite.

[1] Department of Earth System Sciences, Yonsei University, 50 Yonsei-ro Seodaemun-gu, Seoul 03722, Republic of Korea. [2] Division of Geology and Geophysics, Kangwon National University, 1 Gangwondaehak-gil, Chuncheon, Gangwon-do 24341, Republic of Korea. ✉email: changyeol.lee@yonsei.ac.kr

Hydrothermal circulation (HC) affects the thermal structure and hydration of oceanic plates. Despite the decreasing permeability of the oceanic plate over time[1,2], HC occurs even in old oceanic plates (>60 Ma)[3,4]. Especially in subduction zones, bending-related fractures and deep faults that developed in the outer-rise zone allow HC to rejuvenate via increases in permeability and to reach deep oceanic plates[5–7]. The HC in the outer-rise zones redistributes heat energy[8–10] and hydrates the oceanic plate[11,12], which controls the updip depth of the seismogenic zone[13,14] and the water budget of the oceanic plate[15–17].

Heat energy redistribution by the rejuvenated HC is substantiated by densely obtained seafloor heat flow data from the 130-Ma old Pacific plate in the vicinity of the Japan Trench[18,19] (Fig. 1a). Although a seafloor heat flow of 50 mW m^{-2} was expected for the 130-Ma old Pacific plate when heat energy transfer is governed only by heat conduction[20], the measured seafloor heat flow is high up to ~110 mW m^{-2} in the outer-rise zone (i.e., before subduction) (Fig. 1b). Among the possible causes of the high heat flow, heat mining through the rejuvenated HC in the thickening aquifer has been thought to increase the mean seafloor heat flow up to ~73 mW m^{-2} (refs. [8,9,18]); hereafter, the term aquifer indicates the oceanic crust where imbedded fractures and faults increase its permeability. Unlike the relatively well-known roles of HC in the thermal structure and the seafloor heat flow before subduction, those on the overlying accretionary prism and continental crust (i.e., after subduction) have not been quantitatively examined. Although previous studies showed decreased seafloor heat flow after subduction[10,21,22], which may explain the low values of ~20–50 mW m^{-2}, understanding how HC affects the thermal structure and the seafloor heat flow remains unresolved. This is because the studies neglected HC[21,22] or approximated the HC in the subducting oceanic plate by increasing the heat conductivity of the aquifer[10] without self-consistent HC through porous flow.

Along with the characteristic evolution of seafloor heat flow, the remaining amount of magnetization (RAM) of the oceanic plate, coined by Choe and Dyment[23–25], apparently decreases over the convergence distance after the effect of increasing depth of the magnetic sources on the measured magnetic anomalies is considered in the RAM calculation (Fig. 1c and d). Before subduction, the RAM decreases by ~20% over the initial 30-km distance of the outer-rise zone due to the alteration of magnetic minerals by the rejuvenated HC in the thickening aquifer[23,25]. After subduction, the RAM further decreases by ~40% over the 60 km landward distance from the trench where the slab surface reaches 3–10 km depth[24,25]. These studies[24,25] attributed the RAM decrease to the thermal demagnetization of titanomagnetite by postulating that heat mining via persistent HC increases the temperature of the basaltic oceanic crust over the Cuire temperature. However, the postulate is inconsistent with previous studies[13,26] which showed decreased temperature of the subducting oceanic crust by HC. Therefore, the roles of HC in the thermal structure and the seafloor heat flow should be quantitatively evaluated to reveal the cause for the RAM decrease in the vicinity of the Japan Trench.

To quantitatively evaluate the roles of HC in the evolution of seafloor heat flow and RAM, we conducted a series of two-dimensional (2D) numerical model experiments with self-consistent HC through porous flow in the vicinity of the Japan Trench (see the Methods). Our model showed that the rejuvenation and cessation of HC in the basaltic oceanic crust explain the high and low measured seafloor heat flow before and after subduction, respectively. Furthermore, we found that alteration of magnetic minerals in the thickening aquifer causes the RAM decrease before subduction, but thermal demagnetization cannot occur after subduction because the temperature of the oceanic crust is lower than the Curie temperature of the major magnetic carriers in the oceanic crust. Instead, we propose that pressure-driven processes are responsible for the RAM decrease after subduction through demagnetization and phase transition of magnetic minerals, which implies an important role of the increasing pressure in the RAM decreases in other subduction zones.

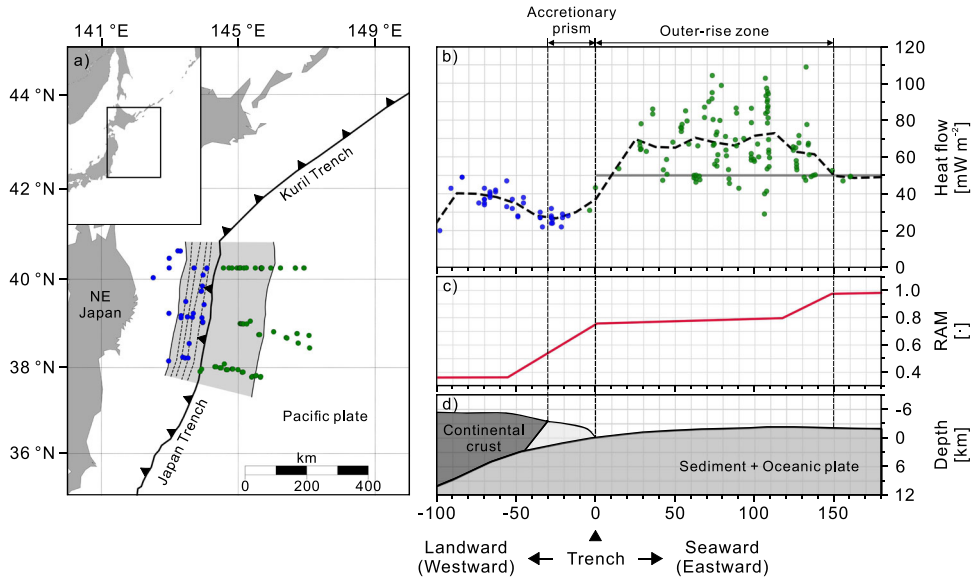

Fig. 1 The measured seafloor heat flow data, remaining amount of magnetization (RAM) of the oceanic plate, and bathymetry profile in the vicinity of the Japan Trench. a Study area between 100 km landward (westward) and 180 km seaward (eastward) from the trench, marked by shading. The values of seafloor heat flow were measured at the green[18] and blue dots[19]. The dashed lines indicate the surface depth of the subducting slab, depicted for every 2 km interval. **b** Measured heat flow data in **a** with their mean values (dashed line) and the expected seafloor heat flow (gray line). The mean values were calculated every 12.5 km by averaging the data within 25 km intervals. **c** RAM in the vicinity of the Japan trench, as demonstrated in Choe and Dyment[25]. **d** Bathymetry profile in the study area[7,54]. The depth of the trench was set to 0 km, and the vertical scale was exaggerated three times for a clear view.

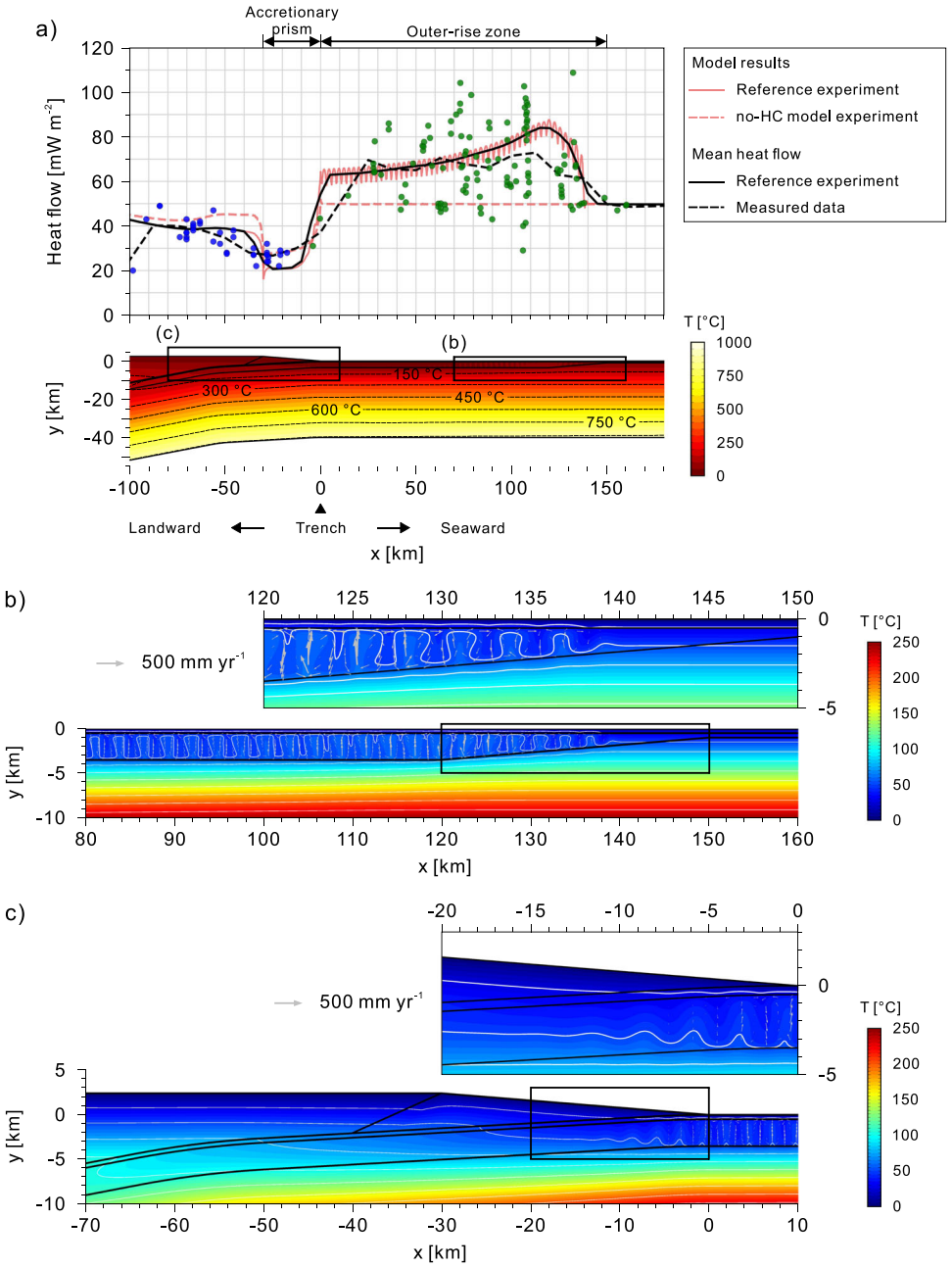

Fig. 2 Results of the model experiment with the measured seafloor heat flow data over the study area between 100 km landward and 180 km seaward from the trench. a The thermal structure and seafloor heat flow calculated using the reference (pink line) and no-HC model (pink dashed line) experiments are plotted together with the measured seafloor heat flow data (green and blue dots) and its mean values (black dashed line) shown in Fig. 1. For comparison, the mean values of the resultant seafloor heat flow using the reference experiment (black line) were calculated every 5 km by averaging the values within 10-km intervals. **b** Rejuvenated hydrothermal circulation in the aquifer and its impact on the thermal structure before subduction. White lines indicate the contours depicted for every 25 °C interval. The porous flow rate in the sediment is too low to be identified by the arrow. **c** Waning hydrothermal circulation in the aquifer and its impact on the thermal structure after subduction. The porous flow rate in the accretionary prism is too low to be identified by the arrow. Other notations are the same as those shown in **b**.

Results and Discussion

Reference experiment. Figure 2 shows the seafloor heat flow, temperature, and porous flow calculated using the numerical model with the values relevant to the vicinity of the Japan Trench (hereafter, reference experiment). The calculated seafloor heat flow increases with periodic variations in the outer-rise zone (before subduction) owing to the rejuvenated HC in the aquifer (Fig. 2a). After subduction, the calculated seafloor heat flow abruptly decreases owing to the cooling effects of the downgoing slab but gradually increases over the convergence distance owing to the frictional heat produced at the slab interface, the increasing effective heat conductivity via the sediment compaction of the accretionary prism, and spatial transition from the accretionary prism to the continental crust on the slab. To clarify the impact of HC on the thermal structure and the resultant seafloor heat flow, an additional model experiment was conducted by assigning a low aquifer permeability to the oceanic crust, which inhibits HC (hereafter, no-HC model experiment). The mean values of the calculated seafloor heat flow using the reference experiment showed good consistency with those of the measured data

compared to those calculated using the no-HC model experiment. A detailed explanation is provided below.

In the oceanic plate before the outer-rise zone ($150 \le x \le 180$ km), HC does not occur in the reference experiment owing to the low aquifer permeability of 10^{-20} m^2 (Fig. 2b). Therefore, the mean temperatures of the aquifer and its top boundary, averaged every 5 km using the values within 10-km intervals, are the same as those calculated using the no-HC model experiment, showing 32.9 and 27.1 °C, respectively. The resultant seafloor heat flow calculated using both model experiments were 49.8 mW m^{-2}.

In the outer-rise zone, the aquifer thickens from 0.5 to 3 km, and its permeability increases from 10^{-20} to 10^{-12} m^2 over the convergence distance of 30 km ($120 \le x < 150$ km), which intensifies the vigor of HC (Fig. 2b and Supplementary Figs. 1a and 2). The mean porous flow rate (averaged every 5 km using the values within 10-km intervals) is 201 mm yr^{-1} at 120 km seaward from the trench. The rejuvenated HC mines the heat energy in the aquifer and transfers it to the overlying sediment. The efficient transport of heat energy decreases the mean temperature of the aquifer but increases the mean temperature of its top boundary over the convergence distance compared to those calculated using the no-HC model experiment. For example, at 120 km seaward from the trench, the mean temperature of the aquifer is 55.2 °C, which is 5.4 °C lower than that calculated using the no-HC model experiment, while the mean temperature of the top boundary of the aquifer is 45.7 °C, which is 18.6 °C higher than that calculated using the no-HC model experiment. The increased temperature of the top boundary of the aquifer increases the mean seafloor heat flow from 49.8 to 83.9 mW m^{-2} over the convergence distance, which is not observed in the no-HC model experiment (Fig. 2a). The hot upwelling and cold downwelling of the convection cells in the aquifer generate periodically varying seafloor heat flow. The wavelength of the seafloor heat flow (i.e., peak-to-peak distance), corresponding to the width of the convection cells, increases from 2.7 to 3.0 km as the aquifer thickens.

After the completion of aquifer thickening ($0 \le x < 120$ km), despite the increased aquifer permeability of 10^{-12} m^2, HC wanes because the heat energy of the deep aquifer was already mined during the previous aquifer thickening stage ($120 \le x < 150$ km). Thus, the mean porous flow rate decreases from 201 to 154 mm yr^{-1} over the convergence distance of 120 km. Although the HC continuously cools down the aquifer, the seafloor heat flow remains higher than that calculated using the no-HC model experiment (Fig. 2a). For example, the mean temperature of the aquifer decreases from 55.2 to 42.6 °C over the convergence distance and is 19.2 °C lower than that calculated using the no-HC model experiment. The mean temperature of the top boundary of the aquifer decreases from 45.7 to 34.3 °C over the convergence distance. However, the resultant mean seafloor heat flow of 63.0 mW m^{-2} is still higher than that calculated using the no-HC model experiment (50.0 mW m^{-2}). The wavelength of the seafloor heat flow decreases from 3.0 to 2.4 km as the plate converges on the trench, indicating that the width of the convection cells decreases.

After subduction, the plate becomes overlain by the accretionary prism over 30 km landward from the trench ($-30 \le x < 0$ km). The accretionary prism increases the effective stress on the aquifer, which decreases the aquifer permeability (Supplementary Fig. 2). Because of the decrease in aquifer permeability, HC wanes and ceases in the aquifer (Fig. 2c). The mean porous flow rates are 13 and 2 mm yr^{-1} at 10 and 20 km landward from the trench, respectively, showing a rapid decrease from 154 mm yr^{-1} at the trench. As a result, the aquifer temperature increases through conduction and shows a monotonous temperature contour rather than periodically varying patterns. At 30 km landward from the trench, the mean temperatures of the aquifer and its top boundary are 66.5 and 56.4 °C, respectively, which are higher than those at the trench (42.6 and 34.3 °C). However, the mean temperatures of the aquifer and its top boundary at the same location are 20.3 and 16.5 °C lower than those calculated using the no-HC model experiment. This is because the aquifer has already lost its heat energy by HC-driven heat mining before subduction. The weak upward porous flow in the accretionary prism (the porous flow rate is <0.8 mm yr^{-1}) by compaction-driven pore water expulsion from the slab sediment transfers heat energy to the seafloor. However, the mean seafloor heat flow of 63.0 mW m^{-2} at the trench decreases to 20.7 mW m^{-2} at 25 km landward from the trench because the cooling effects of the downgoing slab overwhelm the heat transfer through the porous flow. The heat flow value is up to ~8 mW m^{-2} lower than that calculated using the no-HC model experiment because the heat energy of the aquifer was already mined via the HC in the outer-rise zone, which further reduces the heat flow.

Next, the plate becomes overlain by the continental crust in the farther landward area ($-100 \le x < -30$ km). Because the decreasing aquifer permeability due to the increased effective stress halts HC, heat energy is transferred only through conduction in the aquifer. At 100 km landward from the trench, the mean temperatures of the aquifer and its top boundary increase to 177.0 and 157.5 °C, respectively. However, they are still 13.2 and 14.8 °C lower than those calculated using the no-HC model experiment, respectively. At the same location, the mean seafloor heat flow of the overlying continental crust is 42.8 mW m^{-2}, which is only 2.2 mW m^{-2} lower than that calculated using the no-HC model experiment (45.0 mW m^{-2}). This is because the conduction-dominated continental crust overshadows the temperature differences (Fig. 2a).

Parametric tests. The mean seafloor heat flow calculated using the reference experiment explains the measured seafloor heat flow in the vicinity of the Japan Trench. However, changes in the parameters, which are not well constrained, may affect the HC in the aquifer and the resultant seafloor heat flow. Here, we varied each parameter by keeping the other parameters the same as in the reference experiment and examined their impacts on the heat flow.

First, we varied the final aquifer thickness (d_a) as 1, 2, 4, and 5 km, (reference value = 3 km). As d_a constrains the maximum depth from which heat energy is mined to the seafloor via the HC in the aquifer, changes in d_a values affect the mean temperature of the top boundary of the aquifer and the resultant seafloor heat flow. Before subduction, thinner aquifers (the cases using d_a values of 1 and 2 km) result in low mean temperatures at the top boundary of the aquifer, and the resultant mean seafloor heat flow is lower than that calculated using the reference experiment, while the reverse is true when d_a values of 4 or 5 km are used (Fig. 3a). After subduction, when d_a values of 1 or 2 km are used, the mean seafloor heat flow becomes higher than that calculated using the reference experiment because the aquifer loses less heat energy via the HC before subduction. Despite the considerable heat energy loss in the aquifer before subduction, the experiments using d_a values of 4 or 5 km show a higher mean heat flow around the trench after subduction. This is because the thick aquifer allows HC to persist around the trench after subduction. However, HC finally ceases owing to decreasing permeability, and the aquifer that lost more heat energy yields a mean seafloor heat flow lower than that calculated using the reference experiment in the farther landward area.

Next, we evaluated the impact of the initial aquifer permeability (K_{a0}) on the seafloor heat flow. We varied K_{a0} values to 10^{-13}, 5×10^{-13}, 5×10^{-12}, and 10^{-11} m^2 (reference value = 10^{-12} m^2)

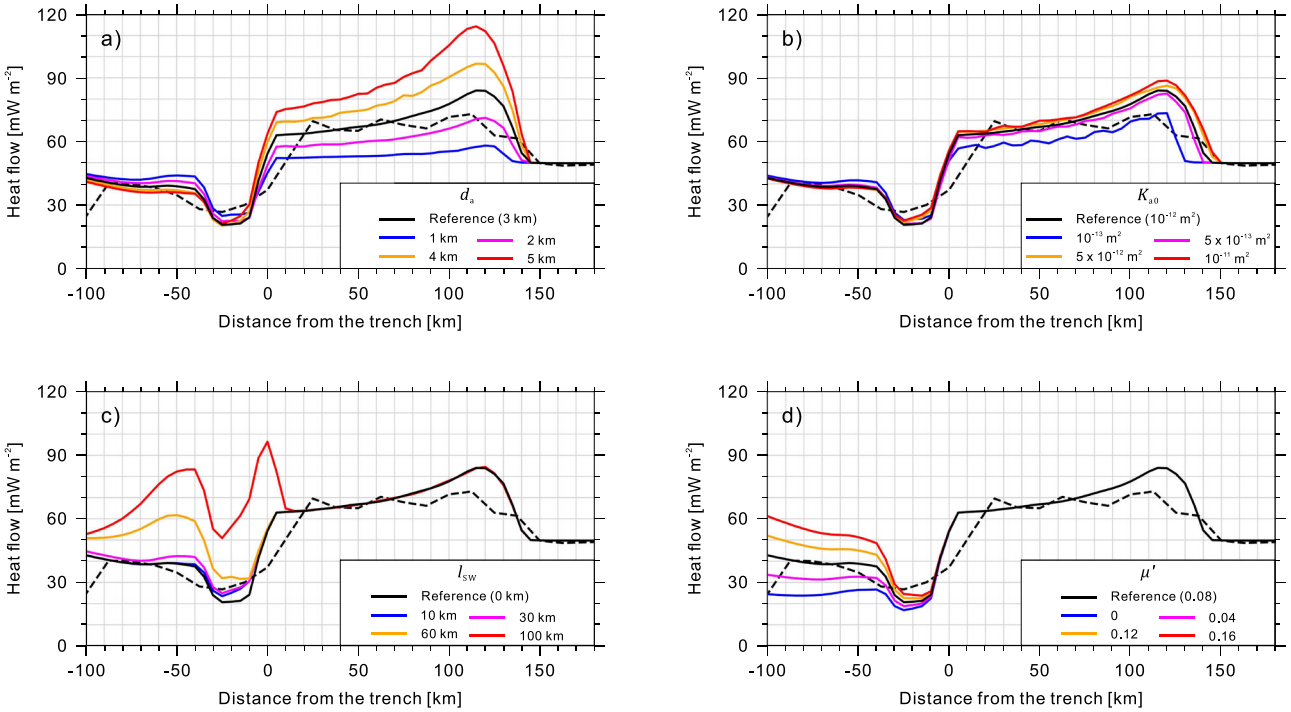

Fig. 3 Calculated mean seafloor heat flow by varying the model parameters, depicted with the value calculated using the reference experiment. The black dashed line indicates the mean values of the measured data described in Fig. 1. The mean values of the resultant seafloor heat flow by varying the model parameters were calculated every 5 km by averaging the values within 10-km intervals. **a** Calculated mean seafloor heat flow values by varying the final aquifer thickness (d_a). **b** Calculated mean seafloor heat flow values by varying the initial aquifer permeability (K_{a0}). **c** Calculated mean seafloor heat flow of the seafloor by varying the landward extent of the zone of gradual permeability decrease (l_{SW}). **d** Calculated mean seafloor heat flow values by varying the effective coefficient of friction (μ').

(Supplementary Fig. 2a). K_{a0} values control the onset location of HC in the outer-rise zone; larger K_{a0} values result in farther onset locations of HC from the trench (Fig. 3b). Because weak HC mines less heat energy in the aquifer, the calculated mean temperatures of the top boundary of the aquifer and the resultant seafloor heat flows in the experiments using the smaller K_{a0} values of 10^{-13} and 5×10^{-13} m^2 are lower than those calculated using the reference experiment, while the reverse is true when the larger K_{a0} values of 5×10^{-12} or 10^{-11} m^2 are used. However, the impact of the initial aquifer permeability on the mean seafloor heat flow is not substantial if the aquifer permeability is $>10^{-13}$ m^2, which is sufficiently high to mine heat energy from the aquifer via vigorous HC. Despite the larger heat energy loss before subduction, the calculated mean seafloor heat flow on the accretionary prism is higher in the experiments using the larger K_{a0} values of 5×10^{-12} and 10^{-11} m^2 than that calculated using the reference experiment because the high permeability allows HC to persist around the trench after subduction. However, the mean seafloor heat flow is not substantially affected by the permeability because conduction dominates the heat energy transfer in the aquifer after subduction as the aquifer permeability decreases.

Third, we evaluated the impact of the persisting HC in the aquifer on the seafloor heat flow after subduction by varying the landward extent of the zone of gradual permeability decrease (l_{SW}) to 10, 30, 60, and 100 km (reference value = 0 km) (Supplementary Fig. 2b). Before subduction, when l_{SW} values of 10, 30, and 60 km are used, the mean seafloor heat flow values calculated using the experiments are the same as those calculated using the reference experiment (Fig. 3c). After subduction, when l_{SW} values of 10 or 30 km are used, the HC maintains heat mining in the aquifer beneath the accretionary prism. As a result, the mean temperature of the top boundary of the aquifer is higher than that calculated using the reference experiment, but the resultant seafloor heat flow values on the continent are similar to those calculated using the reference experiment because the temperature increases are overshadowed by the conduction-dominated continent. When an l_{SW} value of 60 km is used, large-scale HC occurs along the subducting aquifer[13,14]. The HC mines heat energy from the deep subducting slab and increases the mean temperature at the top boundary of the aquifer, which affects the mean seafloor heat flow on the accretionary prism and continental crust. However, the HC transfers heat energy toward only 10 km landward from the trench because HC is not sufficiently vigorous for farther extents. When an l_{SW} of 100 km is used, a more vigorous along-aquifer HC substantially increases the mean temperature of the top boundary of the aquifer and transfers the heat energy farther 10 km seaward from the trench. As a result, the calculated seafloor heat flow demonstrates a narrow peak around the trench before subduction.

Finally, we varied the effective coefficient of friction (μ') to 0, 0.04, 0.12, and 0.16 (reference value = 0.08) (Fig. 3d). Before subduction, the mean seafloor heat flows are the same as those calculated using the reference experiment because the parameter controls only the frictional heat production at the slab interface. After subduction, less frictional heat energy is produced at the slab interface than in the reference experiment when μ' values of 0 and 0.04 are used, while more heat energy is produced when μ' values of 0.12 and 0.16 are used. As a result, the mean seafloor heat flow after subduction increases with the μ' value owing to the higher mean temperature beneath the accretionary prism and continental crust.

Roles of HC in the thermal structure in the vicinity of the Japan Trench. The roles of HC in the thermal structure before subduction are clarified by heat mining in the aquifer, which

increases the mean seafloor heat flow (Fig. 2a). Parametric tests show that the final aquifer thickness (d_a) is a major factor controlling the mean seafloor heat flow before subduction[8] (Fig. 3a). The consistency between the mean seafloor heat flow calculated using the reference experiment and the mean values of the measured data reveals a d_a of 3 km, which was constrained by a seismic survey[7]. Parametric tests also show that the initial aquifer permeability before subduction (K_{a0}) does not substantially affect the magnitude of the mean seafloor heat flow once the value is $>10^{-13}$ m^2 (ref. [8]) (Fig. 3b).

After subduction, the mean seafloor heat flow is decreased owing to the cooling effects of the downgoing slab and is increased over the convergence distance owing to the frictional heat produced at the slab interface, the increasing effective heat conductivity via the sediment compaction, and transition from the accretionary prism to the continental crust on the slab; the combined effects explain the measured data (Fig. 2a). The abrupt lithology transition from the accretionary prism to the continental crust in the model causes the sharp increase in the seafloor heat flow at 30 km landward from the trench, which can be weakened if a gradual transition is considered. Parametric tests show that the extended zone of gradual permeability decrease (l_{SW} values of 60 and 100 km) after subduction allows the HC to mine and transfer heat energy from the deep subducting slab toward the trench, resulting in the high mean seafloor heat flow in the trench and nearby (Fig. 3c). However, the calculated seafloor heat flow values are inconsistent with the mean values of the measured data (Fig. 3c), indicating that heat energy transfer through the HC after subduction is not required[8,10]. Parametric tests also show that the seafloor heat flow calculated using the effective coefficient of friction (μ') of 0.08 explains the mean values of the measured heat flow data (Fig. 3d). The μ' of 0.08 is >0.025, which was suggested by a previous numerical modeling study without HC[27]. This indicates that the heat loss through heat mining in the aquifer before subduction should be considered to constrain the thermal structure and resultant seafloor heat flow in the vicinity of the Japan Trench.

The highly fluctuating measured seafloor heat flow is attributed to the local heterogeneities in the oceanic plate; the geometry of the sediment–aquifer interface and high-permeability fractures and faults developed in the sediment and aquifer may cause local seafloor heat flow anomalies[8,9]. After subduction, the conduction-dominated accretionary prism and continental crust overshadows the thermal structure of the oceanic plate and results in relatively smaller fluctuations in the measured seafloor heat flow. If local heterogeneities are considered in our model, we can further constrain the thermal structure in the vicinity of the Japan Trench.

Possible causes of the decrease in the RAM in the vicinity of the Japan Trench. Previous studies[23–25] attributed the decreases in the RAM in the vicinity of the Japan Trench before and after subduction to the alteration of magnetic minerals and thermal demagnetization of titanomagnetite in the oceanic crust, respectively. Instead of the qualitative speculation, we propose a quantitative explanation for the RAM decreases in the vicinity of the Japan Trench that is consistent with our model results.

We first adopted the assumptions used in previous studies[23–25]; the homogeneously distributed ferromagnetic minerals in the 1-km thick basaltic crust and 5-km thick gabbroic crust only contribute to the RAM, neglecting other geological components that have negligible amounts of ferromagnetic minerals (Fig. 4). When oceanic crust is formed at the mid-ocean ridge, the major magnetic carriers responsible for the RAM are titanomagnetite and magnetite in basaltic and gabbroic crusts, respectively[28]. However, the titanomagnetites in the 0.5-km-thick aquifer might be fully altered to titanomaghemites before reaching the outer-rise zone[29,30] (Fig. 4a and b). The whole RAM of the entire oceanic crust before reaching the outer-rise zone (1.000) is contributed by basaltic (0.400) and gabbroic (0.600) oceanic crusts[31]. Considering that the alteration of titanomagnetites to titanomaghemite can decrease the original magnetization by 40% (ref. [32]), the RAM of the 0.5-km-thick upper and lower basaltic crusts can be decomposed into 0.150 (40% lower than that of the unaltered titanomagnetite of 0.250) and 0.250, respectively (Fig. 4b).

As shown in Fig. 4a, the aquifer thickens to 3 km when the oceanic plate passes over the convergence distance of 30 km in the outer-rise zone[7]. Despite the hydration of the mafic oceanic crust, which potentially accompanies serpentinization, magnetite does not form because the temperature of the oceanic crust is <200 °C (refs. [33,34]). Thus, low-temperature alteration via the HC decreases the magnetization[35,36]. In detail, the lower 0.5-km-thick basaltic oceanic crust loses 40% of its magnetization when titanomagnetite is altered to titanomaghemite[32], decreasing its RAM from 0.250 to 0.150 over the convergence distance. Over the same convergence distance, the upper 2-km-thick gabbroic oceanic crust loses 20% of its magnetization when magnetite is altered to maghemite[37], decreasing its RAM from 0.240 to 0.192 (Fig. 4c). This indicates that the aquifer thickening and coeval mineral alterations in the outer-rise zone are completed at ~120 km from the trench[23,25], which is consistent with the seismic survey[7].

Previous studies[24,25] attributed the decrease in the RAM after subduction to the thermal demagnetization of titanomagnetite in the basaltic oceanic crust when the subducting slab is heated above its Curie temperature of 150 °C owing to the persisting HC. However, this idea should be negated for two reasons. First, the major magnetic carrier in the 130-Ma old basaltic oceanic crust is not titanomagnetite but titanomaghemite, owing to the low-temperature alteration, as shown in previous studies[29,30] and above. Because titanomaghemite has high Curie temperatures of 300–400 °C (refs. [29,38]), no decrease in the RAM due to thermal demagnetization of titanomaghemite occurs in the cold basaltic oceanic crust (<100 °C) owing to HC cessation. Second, even if the major magnetic carrier in the basaltic oceanic crust is titanomagnetite, its Curie temperature should be in the range of 350–500 °C when it carries sufficient magnetization[39]; no decrease in the RAM occurs in the cold basaltic oceanic crust. Therefore, thermal demagnetization after subduction is implausible, and an alternative explanation should be suggested.

Laboratory experiments have shown that the natural remanent magnetization (NRM) of titanomaghemite decreases with increasing pressure. For example, the magnetization of basaltic oceanic crust carried by titanomaghemite decreases by ~50% at 240 MPa (refs. [40,41]), similar to the pressure on the basaltic oceanic crust overlain by the ~5 km thick seawater, ~6-km thick continental crust, and 0.5-km thick sediment 60 km landward from the trench in our model experiment. Consequently, the RAM of the 1-km-thick basaltic oceanic crust decreases by 0.150 over a convergence distance of 60 km after subduction (Fig. 4d). Maghemite in the upper gabbroic oceanic crust is likely transformed to hematite, supported by the fact that the pressure lowers the temperature required for the inversion of maghemite to hematite to room temperature[42,43]. The NRM intensity of the canted-antiferromagnetic hematite was negligible compared to that of ferrimagnetic maghemite. Thus, the inversion decreases the RAM of the upper 2-km-thick gabbroic oceanic crust from 0.192 to nearly zero (Fig. 4d). The increasing pressure also decreases the NRM intensity carried by magnetite in the lower 3-km gabbroic oceanic crust by ~15% (refs. [44,45]), decreasing the

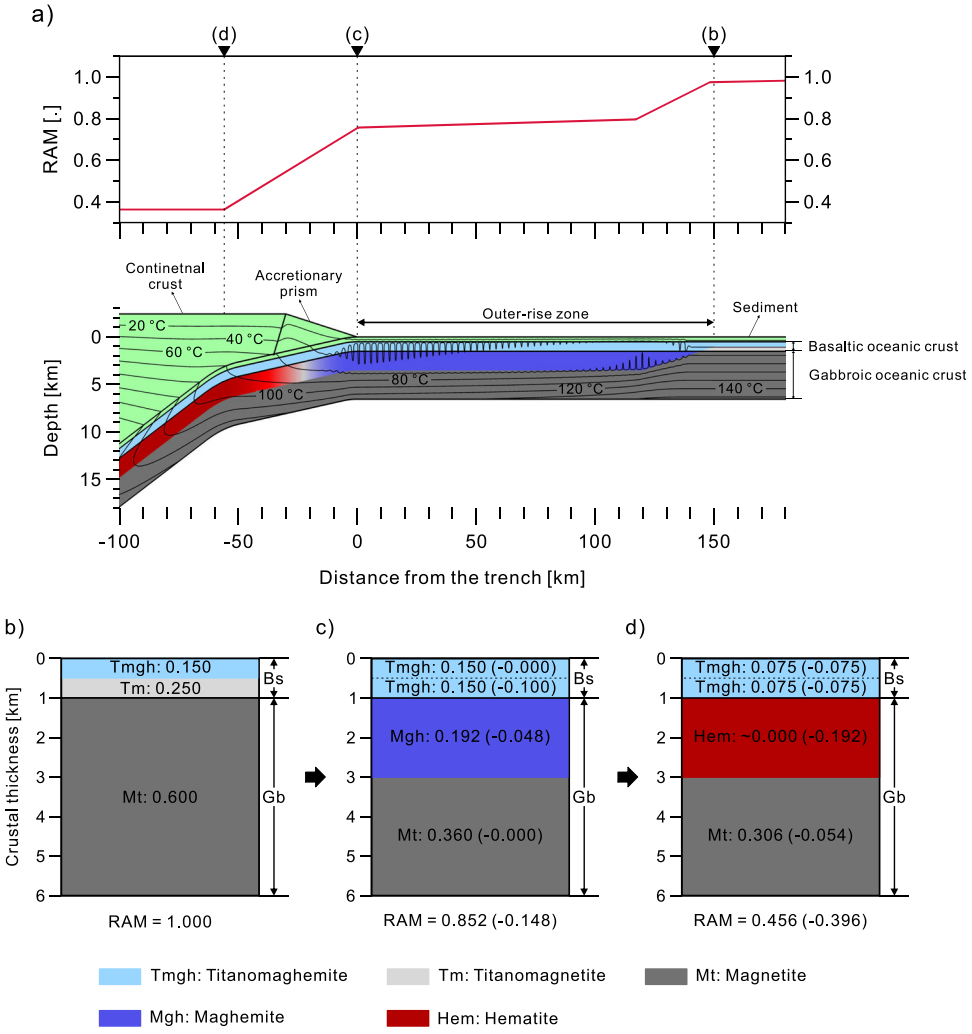

Fig. 4 Thermal structure and major magnetic carriers of the oceanic crust in the study area with the decreasing remaining amount of magnetization (RAM). a Thermal structure calculated using the reference experiment and representative magnetic minerals with the decreasing RAM. The model geometry was vertically exaggerated four times for a clear view. The black lines indicate the temperature contour depicted for every 20 °C interval. The greenish area (sediment, accretionary prism, and continental crust) does not contribute to the RAM. The major magnetic carriers of the basaltic and gabbroic oceanic crusts are titanomagnetite (light gray) and magnetite (dark gray), respectively. The bluish area indicates where these magnetic minerals are altered by hydrothermal circulation (HC) (light blue and blue for titanomaghemite and maghemite, respectively). The reddish area indicates the hematite transformed from maghemite by increasing pressure. **b**–**d** Distributions of major magnetic carriers and the RAM in the oceanic crust. The abbreviations Bs and Gb indicate basaltic and gabbroic oceanic crusts, respectively. The *y*-axis indicates the depth from the top of the oceanic crust (top boundary of the aquifer). The values in parentheses represent the decreased RAM from the previous stage.

RAM of the lower gabbroic oceanic crust from 0.360 to 0.306. As a result, the RAM of the whole oceanic crust decreases by 0.396 over the convergence distance, which is consistent with the observed RAM decrease of 0.4 after subduction. Although the modeled RAM decrease before subduction (0.148) is smaller than the observed RAM decrease (0.2), further consideration of other factors, such as self-reversal during alteration[46] and chemical remanent magnetization acquisition[28,47], may accommodate the RAM discrepancy. Although thermal demagnetization could explain the RAM decrease in young subduction zones such as Cascadia, the suggested pressure-driven processes after subduction likely explain the RAM decreases observed in other subduction zones (e.g., Alaska, and Izu–Bonin–Mariana) regardless of the age and convergence rate of the subducting slab[25,48].

Methods

Governing equations. The HC calculation requires simultaneous calculations of the porous flow and heat energy transfer using continuity, Darcy's, and energy equations[26] over the model domain, which consists of sediment, oceanic plate (aquifer and basement), accretionary prism, and continental crust (Supplementary Fig. 1a).

$$\nabla \cdot \mathbf{u} + \nabla \cdot (\phi \mathbf{V}) = 0 \tag{1}$$

$$\mathbf{u} = -\frac{K}{\mu_f}(\nabla p + \rho_f \mathbf{g}) \tag{2}$$

$$(\rho c_p)_{eff}\frac{\partial T}{\partial t} = -(\rho c_p)_{eff}\mathbf{V} \cdot \nabla T - (\rho c_p)_f \mathbf{u} \cdot \nabla T + \nabla \cdot (k_{eff}\nabla T) + H \tag{3}$$

where $\mathbf{u}$ indicates the pore water velocity; ϕ is the porosity; $\mathbf{V}$ is the convergence velocity; K is the isotropic permeability; μ_f is the pore water viscosity; p is the pore water pressure; ρ_f is the pore water density; $\mathbf{g}$ is the gravitational acceleration; ρc_p is the heat capacity; T is the temperature; t is the time; k is the heat conductivity; and H is the heat source which includes the frictional heat produced at the slab interface after subduction and radiogenic heat produced in the sediment, accretionary prism, and continental crust. The effective heat capacity and conductivity of the sediment, oceanic plate, and accretionary prism are defined as follows:

$$(\rho c_p)_{eff} = \phi(\rho c_p)_f + (1-\phi)(\rho c_p)_m \tag{4}$$

$$k_{eff} = k_f^{\phi} k_m^{(1-\phi)} \tag{5}$$

where the subscripts f and m indicate the pore water and the matrix of the porous media, respectively[49,50]. Notably, m can be replaced by s, op, or ap for sediment, oceanic plate, and accretionary prism, respectively. For simplicity, the same thermodynamic properties were used for the oceanic plate, which is composed of basaltic oceanic crust, gabbroic oceanic crust, and lithospheric mantle. The relevant parameters are listed in Supplementary Table 1.

The temperature-dependent density (ρ_f) and viscosity (μ_f) of pore water can be approximated as follows:

$$\rho_f = \rho_{f0}(1 - \alpha_0 T - \alpha_1 T^2) \quad (6)$$

$$\mu_f = 2.414 \times 10^{-5} \exp\left(\frac{570.58}{T[^\circ C^{-1}] + 133.15}\right)[\mathrm{Pa\,s}] \quad (7)$$

where ρ_{f0} is the pore water density at 0 °C and α_0 and α_1 are the first and second coefficients of the thermal expansivity of the pore water, which are 1.367×10^{-4} °C^{-1} and 2.159×10^{-6} °C^{-2}, respectively[8]. The effect of pressure on the density and viscosity of pore water was not considered for simplicity.

The rate of frictional heating per unit area produced at the slab interface after subduction (q_f) was calculated as follows[27]:

$$q_f = \mu' \sigma_n |\mathbf{V}| \quad (8)$$

where μ' is the effective coefficient of friction and σ_n is the normal stress by the overlying accretionary prism and continental crust calculated by their weights[27]. We used the μ' value of 0.08, consistent with the experimental value of the saturated montmorillonite–granite assemblage[51].

The sediment and oceanic plate kinematically converged to the trench at a rate of 9 cm yr^{-1}, but the accretionary prism was stationary ($\mathbf{V} = 0$) because only a small amount of the incoming sediment had accumulated in the accretionary prism[21]. For the stationary and low-permeability (10^{-20} m^2) continental crust, the convergence velocity and pore water velocity were set to 0 m s^{-1}. Thus, heat conduction was considered only in the energy equation (Eq. 3) using the effective thermodynamic properties, i.e., $(\rho c_p)_c$ and k_c (refs. [10,52,53]).

Model setup. In the 2D numerical model, we used a trench-normal cross-section of the vicinity of the Japan Trench, which extends from 250 km seaward (eastward) to 160 km landward (westward) from the Japan Trench (Supplementary Fig. 1a). The model length was large enough to minimize the boundary effects compared to the study area (from 180 km seaward to 100 km landward from the trench, Fig. 1), from which the heat flow and RAM data were obtained. Before subduction, the 0.5 km-thick sediment[7] overlies the oceanic plate, of which the 39.5 km-thick upper portion is considered only for simplicity. The oceanic plate is initially composed of a 0.5-km-thick aquifer and 39 km-thick basement before the outer-rise zone ($x > 150$ km). The aquifer thickens downward from 0.5 to 3 km (d_a) from 150 to 120 km seaward from the trench due to fracturing and faulting developed by plate bending[7]. The model geometry after subduction was expressed as a combination of straight and curved slabs, consistent with the slab geometry[54,55].

The porosity of the sediment decreases as its depth from the seafloor (z) increases, owing to sediment compaction. Thus, the depth-dependent porosity ($\phi_s(z)$) derived from a previous study[56] was used as follows:

$$\phi_s(z) = 0.6932 \exp(-0.525 z[\mathrm{km}^{-1}]) \quad (9)$$

As the decreased sediment porosity decreases its permeability, the porosity-dependent permeability of the sediment (K_s) defined by the Konzeny–Carman equation[57] was used as follows:

$$K_s = \frac{[\phi_s(z)]^3}{[5 s_0^2 (1 - \phi_s(z))^2]} \quad (10)$$

where an s_0 value of 3.84×10^8 m^{-1} was used for the maximum permeability of 10^{-17} m^2 at the seafloor (depth of 0 km)[56]. The minimum permeability was set to 10^{-20} m^2, where the porous flow was negligible[58,59]. Unlike the sediment, the porosity of the oceanic plate (aquifer and basement) was set to 0.1 owing to its small value[9]. Before subduction, aquifer permeability increases from 10^{-20} to 10^{-12} m^2 (K_{a0}) (ref. [60]) from 150 to 120 km seaward from the trench, where the aquifer thickens due to fracturing and faulting developed by plate bending (Supplementary Fig. 2). After subduction, a decrease in the aquifer permeability from the initial value (K_{a0}) with increasing depth was considered. Spinelli and Wang[13] showed that a gradual decrease in aquifer permeability with increasing depth allows HC to persist in the aquifer after subduction. However, the experimental dataset showed that the aquifer permeability rapidly decreases with depth[61]. To examine the HC in the aquifer after subduction, we defined aquifer permeability (K_a) by varying the landward extent of the zone of gradual aquifer permeability decrease (l_{SW}), as follows:

$$\log(K_a[\mathrm{m}^{-2}]) = \log(K_{a0}[\mathrm{m}^{-2}]) \quad (0 \le x < 180\ \mathrm{km}) \quad (11a)$$

$$\log(K_a[\mathrm{m}^{-2}]) = \log(K_{a0}[\mathrm{m}^{-2}]) - 0.04(z - z_0)[\mathrm{km}^{-1}] \quad (-l_{SW} \le x < 0\ \mathrm{km}) \quad (11b)$$

$$\log(K_a[\mathrm{m}^{-2}]) = \log(K'_{a0}[\mathrm{m}^{-2}]) - 0.639(\ln(\sigma_e[\mathrm{MPa}^{-1}]) - \ln(\sigma_0[\mathrm{MPa}^{-1}])) \quad (-100\ \mathrm{km} \le x < -l_{SW}) \quad (11c)$$

where z_0 is the initial depth to the bottom boundary of the sediment before subduction (0.5 km); K'_{a0} is the aquifer permeability at the landward extent of the zone of gradual permeability decrease ($x = -l_{SW}$); σ_e is the total effective stress generated by the overlying continental crust, accretionary prism, and sediment; and σ_0 is the σ_e value at the landward margin of the zone of gradual permeability decrease ($x = -l_{SW}$). σ_e can be approximated by neglecting the small density change with temperature, as follows:

$$\sigma_e = (\rho_c - \rho_{f0})|\mathbf{g}| \int_0^{z_1} (1 - \phi_c) dz + (\rho_{ap} - \rho_{f0})|\mathbf{g}| \int_{z_1}^{z_2} (1 - \phi_{ap}(z)) dz + (\rho_s - \rho_{f0})|\mathbf{g}| \int_{z_2}^{z_3} (1 - \phi_s(z)) dz \quad (12)$$

where z_1 and z_2 are the depths to the top and bottom boundaries of the accretionary prism, respectively, and z_3 is the depth to the bottom boundary of the subducting sediment. The reference l_{SW} value was 0 km, which did not allow for a slow decrease in permeability, consistent with the experiments[61] (Supplementary Fig. 2). The minimum K_a value was set to 10^{-20} m^2.

The accretionary prism was assumed to have the same porosity ($\phi_{ap}(z) = \phi_s(z)$) and permeability ($K_{ap} = K_s$) as the sediment. The radiogenic heat productions in the sediment (γ_s) and accretionary prism (γ_{ap}) were 1.5 and 1.8 μW m^{-3}, respectively[62,63], while the heat production in the oceanic plate was neglected because of its small contribution. For the upper and lower continental crusts, radiogenic heat productions of 1.3 (γ_{c1}) and 0.27 μW m^{-3} (γ_{c2}) were used, respectively, with a 1-km thick transition zone at a depth of 15 km from the seafloor[54].

To calculate the continuity and Darcy's equations, the hydrostatic pressure (p_0) by the overlying seawater was defined at the seafloor as a constant pressure boundary condition (Supplementary Fig. 1b). By assuming that the depth to the seafloor from sea level before subduction is 7 km, p_0 can be defined as follows:

$$p_0 = \rho_{f0}|\mathbf{g}|(7[\mathrm{km}] - y) \quad (13)$$

At the other boundaries of the model, a no-flow boundary condition was prescribed. To solve the energy equation, a constant temperature of 0 °C was assigned to the seafloor (Supplementary Fig. 1c). At the bottom of the model, the basal heat flow calculated using the large-scale thermomechanical model of the Northeast Japan subduction zone was assigned at the bottom of the model[64], with the proper parameter values for the Northeast Japan subduction zone. At the seaward vertical boundary of the model, a temperature profile yielding a surface heat flow of ~50 mW m^{-2} was assigned, while an outflow boundary condition was assigned at the landward vertical boundary.

The model performs in two steps. First, the energy equation (Eq. 3) was solved without porous flow ($u = 0$) for 100 Myr to determine the semi-steady-state temperature distribution. Second, the porous flow was considered for 5 Myr, which is long enough for the converging plate to reach 100 km landward from the trench to find the semi-steady-state porous flow. The temperature distribution calculated in the first step and the hydrostatic pressure were used as the initial temperature and pressure conditions, respectively. To increase the model stability, the aquifer permeability was gradually increased from 10^{-20} m^2 to K_a for 1 Myr (from 0.25 to 1.25 Myr). However, a constant value of 10^{-20} m^2 was used in the no-HC model experiment for the entire model calculation.

Meshes and solver. The model was decomposed into 175,554 unstructured triangular elements (Supplementary Fig. 1d). To closely monitor the porous flow, fine meshes were used for the sediment, aquifer, and accretionary prism, and coarse meshes were used for the low-permeability subdomains (basement and continental crust). A maximum element size of 0.3 km was set for the sediment and accretionary prism, 0.15 km was set for the aquifer, 6 km was set for the basement, and 2.25 km was set for the continental crust.

The governing equations with the model meshes were solved using the commercial finite-element package COMSOL Multiphysics® (ver. 5.5). A direct multifrontal massively parallel sparse (MUMPS) solver was used for all the model calculations. The generalized-alpha method automatically determined the time step when only the energy equation was solved. The maximum time step was set to 500 year to guarantee model stability when the porous flow was simultaneously evaluated. If necessary, a smaller maximum time step of 100 or 300 year was used for model stability.

Data availability

Data used in this study can be found in the published literatures and cited references. All numerical model results used in this study are available on an open repository, Zenodo: https://doi.org/10.5281/zenodo.8000635.

Code availability

The commercial software can be accessed to www.comsol.com.

Received: 11 November 2022; Accepted: 19 June 2023;
Published online: 04 July 2023

References

1. Becker, K. & Fisher, A. T. Permeability of upper oceanic basement on the eastern flank of the Juan de Fuca Ridge determined with drill-string packer experiments. *J. Geophys. Res. Solid Earth* **105**, 897–912 (2000).
2. Becker, K. & Davis, E. E. New evidence for age variation and scale effects of permeabilities of young oceanic crust from borehole thermal and pressure measurements. *Earth Planet. Sci. Lett.* **210**, 499–508 (2003).
3. Fisher, A. T. Marine hydrogeology: recent accomplishments and future opportunities. *Hydrogeol. J.* **13**, 69–97 (2005).
4. Fisher, A. T. & Von Herzen, R. P. Models of hydrothermal circulation within 106 Ma seafloor: Constraints on the vigor of fluid circulation and crustal properties, below the Madeira Abyssal Plain. *Geochem. Geophys. Geosyst.* https://doi.org/10.1029/2005GC001013 (2005).
5. Contreras-Reyes, E., Grevemeyer, I., Flueh, E. R., Scherwath, M. & Heesemann, M. Alteration of the subducting oceanic lithosphere at the southern central Chile trench–outer rise. *Geochem. Geophys. Geosyst.* https://doi.org/10.1029/2007GC001632 (2007).
6. Shillington, D. J. et al. Link between plate fabric, hydration and subduction zone seismicity in Alaska. *Nat. Geosci.* **8**, 961–964 (2015).
7. Fujie, G. et al. Controlling factor of incoming plate hydration at the north-western Pacific margin. *Nat.Commun.* **9**, 1–7 (2018).
8. Kawada, Y., Yamano, M. & Seama, N. Hydrothermal heat mining in an incoming oceanic plate due to aquifer thickening: Explaining the high heat flow anomaly observed around the Japan Trench. *Geochem. Geophys. Geosyst.* **15**, 1580–1599 (2014).
9. Ray, L., Kawada, Y., Hamamoto, H. & Yamano, M. Multiple-scale hydrothermal circulation in 135 Ma oceanic crust of the J apan T rench outer rise: Numerical models constrained with heat flow observations. *Geochem. Geophys. Geosyst.* **16**, 2711–2724 (2015).
10. Lucero, A., Spinelli, G. & He, J. The thermal effects of plate-bending-related thickening of the oceanic crustal aquifer in the Nankai trough and Japan Trench subduction zones. *J. Geophys. Res. Solid Earth* **124**, 1205–1221 (2019).
11. Peacock, S. M. Are the lower planes of double seismic zones caused by serpentine dehydration in subducting oceanic mantle? *Geology* **29**, 299–302 (2001).
12. Hatakeyama, K., Katayama, I., Hirauchi, K.-I. & Michibayashi, K. Mantle hydration along outer-rise faults inferred from serpentinite permeability. *Sci. Rep.* **7**, 1–8 (2017).
13. Spinelli, G. A. & Wang, K. Effects of fluid circulation in subducting crust on Nankai margin seismogenic zone temperatures. *Geology* **36**, 887–890 (2008).
14. Kummer, T. & Spinelli, G. A. Hydrothermal circulation in subducting crust reduces subduction zone temperatures. *Geology* **36**, 91–94 (2008).
15. Hacker, B. R. H_2O subduction beyond arcs. *Geochem. Geophys. Geosyst.* https://doi.org/10.1029/2007GC001707 (2008).
16. Till, C. B. A review and update of mantle thermobarometry for primitive arc magmas. *Am. Mineral.* **102**, 931–947 (2017).
17. Lee, C., Seoung, D. & Cerpa, N. G. Effect of water solubilities on dehydration and hydration in subduction zones and water transport to the deep mantle: Implications for natural subduction zones. *Gondwana Res.* **89**, 287–305 (2021).
18. Yamano, M., Hamamoto, H., Kawada, Y. & Goto, S. Heat flow anomaly on the seaward side of the Japan Trench associated with deformation of the incoming Pacific plate. *Earth Planet. Sci. Lett.* **407**, 196–204 (2014).
19. Fuchs, S. et al. *The Global Heat Flow Database: Release 2021. GFZ Data Services.* https://doi.org/10.5880/fidgeo.2021.014 (2021).
20. Turcotte, D. L. & Schubert, G. *Geodynamics* (Cambridge university press, 2002).
21. Wang, K., Hyndman, R. & Davis, E. Thermal effects of sediment thickening and fluid expulsion in accretionary prisms: model and parameter analysis. *J. Geophys. Res. Solid Earth* **98**, 9975–9984 (1993).
22. Wang, K. Kinematic models of dewatering accretionary prisms. *J. Geophys. Res. Solid Earth* **99**, 4429–4438 (1994).
23. Choe, H. & Dyment, J. Decreasing magnetization, lithospheric flexure, and rejuvenated hydrothermalism off the Japan-Kuril subduction zone. *Geophys. Res. Lett.* **47**, e2019GL085975 (2020).
24. Choe, H. & Dyment, J. Fading magnetic anomalies, thermal structure and earthquakes in the Japan Trench. *Geology* **48**, 278–282 (2020).
25. Choe, H. & Dyment, J. The fate of marine magnetic anomaly in subduction zones: a global appraisal. *Earth Planet. Sci. Lett.* **561**, 116787 (2021).
26. Cozzens, B. D. & Spinelli, G. A. A wider seismogenic zone at Cascadia due to fluid circulation in subducting oceanic crust. *Geology* **40**, 899–902 (2012).
27. Gao, X. & Wang, K. Strength of stick-slip and creeping subduction megathrusts from heat flow observations. *Science* **345**, 1038–1041 (2014).
28. Gee, J. S. & Kent, D. V. Source of oceanic magnetic anomalies and the geomagnetic polarity time scale. *Treatise Geophys.* https://doi.org/10.7916/D8DV1V8P (2007).
29. Zhou, W., Van der Voo, R., Peacor, D. R., Wang, D. & Zhang, Y. Low-temperature oxidation in MORB of titanomagnetite to titanomaghemite: A gradual process with implications for marine magnetic anomaly amplitudes. *J. Geophys. Res. Solid Earth* **106**, 6409–6421 (2001).
30. Doubrovine, P. V. & Tarduno, J. A. Alteration and self-reversal in oceanic basalts. *J. Geophys. Res. Solid Earth* https://doi.org/10.1029/2006JB004468 (2006).
31. Pariso, J. E. & Johnson, H. P. Do layer 3 rocks make a significant contribution to marine magnetic anomalies? In situ magnetization of gabbros at Ocean Drilling Program Hole 735B. *J. Geophys. Res. Solid Earth* **98**, 16033–16052 (1993).
32. Marshall, M. & Cox, A. Magnetic changes in pillow basalt due to sea floor weathering. *J. Geophys. Res.* **77**, 6459–6469 (1972).
33. Dyment, J., Arkani-Hamed, J. & Ghods, A. Contribution of serpentinized ultramafics to marine magnetic anomalies at slow and intermediate spreading centres: insights from the shape of the anomalies. *Geophys. J. Int.* **129**, 691–701 (1997).
34. Klein, F. et al. Magnetite in seafloor serpentinite—some like it hot. *Geology* **42**, 135–138 (2014).
35. Ozima, M. Magnetic processes in oceanic ridge. *Earth Planet. Sci. Lett.***13**, 1–5 (1971).
36. Zhu, J. et al. A reduced crustal magnetization zone near the first observed active hydrothermal vent field on the Southwest Indian Ridge. *Geophys. Res. Lett.* https://doi.org/10.1029/2010GL043542 (2010).
37. Johnson, H. P. & Merrill, R. T. Magnetic and mineralogical changes associated with low-temperature oxidation of magnetite. *J. Geophys. Res.* **77**, 334 (1972).
38. Matzka, J., Krása, D., Kunzmann, T., Schult, A. & Petersen, N. Magnetic state of 10–40 Ma old ocean basalts and its implications for natural remanent magnetization. *Earth Planet. Sci.Lett.* **206**, 541–553 (2003).
39. Jackson, M. & Bowles, J. A. Curie temperatures of titanomagnetite in ignimbrites: Effects of emplacement temperatures, cooling rates, exsolution, and cation ordering. *Geochem. Geophys. Geosyst.* **15**, 4343–4368 (2014).
40. Ozima, M., Joshima, M. & Kinosmta, H. Magnetic properties of submarine basalts and the implications on the structure of the oceanic crust. *J. Geomagn. Geoelectr.* **26**, 335–354 (1974).
41. Pozzi, J. Magnetic properties of oceanic basalts—effects of pressure and consequences for the interpretation of anomalies. *Earth Planet. Sci. Lett.* **26**, 337–344 (1975).
42. Kushiro, I. γ→α transition in Fe_2O_3 with pressure. *J. Geomagn. Geoelectr.* **11**, 148–151 (1960).
43. Adnan, J. & O'Reilly, W. The transformation of γ Fe_2O_3 to α Fe_2O_3: Thermal activation and the effect of elevated pressure. *Phys Earth Planet. Inter.* **110**, 43–50 (1999).
44. Mussett, A. Pressure demagnetization of rocks. *Nature* **293**, 609–609 (1981).
45. Pearce, G. W. & Karson, J. A. On pressure demagnetization. *Geophys. Res. Lett.* **8**, 725–728 (1981).
46. Doubrovine, P. V. & Tarduno, J. A. Self-reversed magnetization carried by titanomaghemite in oceanic basalts. *Earth Planet. Sci. Lett.* **222**, 959–969 (2004).
47. Raymond, C. & LaBrecque, J. Magnetization of the oceanic crust: Thermoremanent magnetization of chemical remanent magnetization? *J. Geophys. Res. Solid Earth* **92**, 8077–8088 (1987).
48. Reagan, M., Pearce, J., Petronotis, K. & Scientists, E. Izu-Bonin-mariana fore arc. *Prog. Int. Ocean Discov. Prog.* https://doi.org/10.14379/iodp.proc.352.105.2015 (2015).
49. Harris, R. N., Schmidt-Schierhorn, F. & Spinelli, G. Heat flow along the NanTroSEIZE transect: Results from IODP Expeditions 315 and 316 offshore the Kii Peninsula, Japan. *Geochem. Geophys. Geosyst.* https://doi.org/10.1029/2011GC003593 (2011).
50. Goto, S. et al. Physical and thermal properties of mud-dominant sediment from the Joetsu Basin in the eastern margin of the Japan Sea. *Mar. Geophys. Res.* **38**, 393–407 (2017).
51. Wang, C. Y. & Mao, N. H. Shearing of saturated clays in rock joints at high confining pressures. *Geophys. Res. Lett.* **6**, 825–828 (1979).
52. Wada, I. & Wang, K. Common depth of slab-mantle decoupling: Reconciling diversity and uniformity of subduction zones. *Geochem. Geophys. Geosyst.* https://doi.org/10.1029/2009GC002570 (2009).
53. Peacock, S. M. & Wang, K. Seismic consequences of warm versus cool subduction metamorphism: Examples from southwest and northeast Japan. *Science* **286**, 937–939 (1999).
54. Takahashi, N. et al. Seismic structure and seismogenesis off Sanriku region, northeastern Japan. *Geophys. J. Int.* **159**, 129–145 (2004).
55. Nakajima, J., Tsuji, Y. & Hasegawa, A. Seismic evidence for thermally-controlled dehydration reaction in subducting oceanic crust. *Geophys. Res. Lett.* https://doi.org/10.1029/2008GL036865 (2009).
56. Valdez II, R. D., Lauer, R. M., Ikari, M. J., Kitajima, H. & Saffer, D. M. Data report: permeability and consolidation behavior of sediments from the northern Japan Trench subduction zone, IODP Site C0019. *Proc. IODP* https://doi.org/10.2204/iodp.proc.343343T.201.2015 (2015).

57. Carman, P. C. *Flow of Gases Through Porous Media*. https://www.osti.gov/servlets/purl/1127097 (1956).
58. Manning, C. E., Ingebritsen, S. E. & Bird, D. K. Missing mineral zones in contact metamorphosed basalts. *Am. J. Sci.* **293**, 894–938 (1993).
59. Ingebritsen, S. & Hayba, D. Fluid flow and heat transport near the critical point of H_2O. *Geophys. Res. Lett.* **21**, 2199–2202 (1994).
60. Hutnak, M. et al. Hydrothermal recharge and discharge guided by basement outcrops on 0.7–3.6 Ma seafloor east of the Juan de Fuca Ridge: observations and numerical models. *Geochem. Geophys. Geosyst.* https://doi.org/10.1029/2006GC001242 (2006).
61. Lamur, A. et al. The permeability of fractured rocks in pressurised volcanic and geothermal systems. *Sci. Rep.* **7**, 1–9 (2017).
62. Hyndman, R., Wang, K. & Yamano, M. Thermal constraints on the seismogenic portion of the southwestern Japan subduction thrust. *J. Geophys. Res. Solid Earth* **100**, 15373–15392 (1995).
63. Yamaguchi, T. I., Yamano, M., Nagao, T. & Goto, S. Distribution of radioactive heat production around an active fault and in accretionary prisms of southwest Japan. *Phys. Earth Planet. Inter.* **126**, 269–277 (2001).
64. Yun, T. K. et al. Simulated Evaluations of Hydrothermal Anomaly in Muroto Transect, Nankai Trough, Japan. *Gondwana Res.* https://doi.org/10.1016/j.gr.2022.04.024 (2022).

Acknowledgements

D.H. and C.L. were supported by the National Research Foundation of Korea [grant numbers: 2017R1A6A1A07015374 and 2022R1A2C1004592] and the Yonsei University Research Fund [grant number: 2019-22-0010]. Y.-H.P. was supported by the National Research Foundation of Korea [grant numbers: 2019R1F1A1041293 and 2019R1A6A1A03033167].

Author contributions

D.H.: Conceptualization, Methodology, Investigation, Visualization, Writing—original draft, Writing—review and editing. Y.-H.P.: Conceptualization, Investigation, Writing—review and editing. C.L.: Conceptualization, Investigation, Supervision, Writing—original draft, Writing—review and editing.

Competing interests

The authors declare no competing interests.

Additional information

Supplementary information The online version contains supplementary material available at https://doi.org/10.1038/s43247-023-00903-5.

Correspondence and requests for materials should be addressed to Changyeol Lee.

Peer review information *Communications Earth & Environment* thanks Eric Ferre, Marina Manea and the other, anonymous, reviewer(s) for their contribution to the peer review of this work. Primary Handling Editors: Claire Nichols and Joe Aslin.

Reprints and permission information is available at http://www.nature.com/reprints

Publisher's note Springer Nature remains neutral with regard to jurisdictional claims in published maps and institutional affiliations.